A Cascade-Free Model Predictive Control Scheme for Back-to-Back Converter-Fed PMSM Drive System

Yingjie He, *Member, IEEE*, Ying Tang, *Member, IEEE*, Xiaonan Gao, *Member, IEEE*, Haotian Xie, *Member, IEEE*, Fengxiang Wang, *Senior Member, IEEE*, and Ralph Kennel, *Senior Member, IEEE*

***Abstract*—In this article, a cascade-free model predictive control (MPC) scheme without the outer dc-link voltage control loop is proposed for the back-to-back converter-fed permanent magnet synchronous machine drive system. Specifically, the voltage regulation term is integrated together with the power regulation term into a newly constructed cost function so that the control of dc-link voltage as well as power can be realized by a single cost function. To predict accurately and to reduce the sensitivity to variable parameters, the expressions of dc-link voltage and power are dynamically corrected, thus enhancing the robustness. In addition to presenting no tracking deviation in steady state, the dc-link voltage also presents smaller deviation from reference and faster recovery time in dynamics. It is beneficial to enhancing the reliability of system since the voltage surge on power switches and diodes has been reduced. Besides, controllable power flow, sinusoidal phase current, and well-regulated electromagnetic torque can be achieved in the system as well. A series of experiments are carried out to test the feasibility of the proposed scheme. Performance comparisons with the classical proportional integration controller-based MPC and the modified cascade-free quasi-centralized MPC validate the improvements of the proposed control scheme.**

***Index Terms*—Back-to-back converter, cascade-free model predictive control (MPC), permanent magnet synchronous machine (PMSM).**

I. Introduction

OWING wing to the merits, such as bidirectional energy flow, controllable power factor, sinusoidal grid-side current, adjustable dc-link voltage, high energy conversion efficiency, and full-variable speed operation, the permanent magnet synchronous machine (PMSM)-based back-to-back converters have been an attractive drive topology for wind energy conversion system [1], [2], [3] and industrial drive. The research works of back-to-back converter-fed PMSM system mainly focus on their open-switch fault diagnosis [4], [5], fault-tolerant operation [6], [7], high-performance control scheme [8], [9], etc. For a high-performance control scheme, a pulsewidth modulation strategy is developed in [10] to cancel the common-mode voltage by synchronizing the commutations between grid-side converter (GSC) and machine-side converter (MSC). In [11], the discontinuous space vector pulse width modulation (SVPWM) is adopted to increase system efficiency by reducing the switching action of power devices, and the increased common-mode and phase-to-ground voltages are reduced to values similar to that of the general modulation method. In [12], a hysteresis current controller is adopted to control MSC and GSC, but power tracking errors exist due to the inaccurate model. The proportional–integral (PI) controller-based double closed-loop control method is the most classical. In this scheme, an outer voltage PI controller is applied to generate power/current reference, and the inner feedforward decoupling controller is applied to achieve reference tracking [13]. However, this linear controller has a limited bandwidth, which tends to present a slow dynamic response. To accelerate the dynamic response, direct power control and direct torque control, which directly selects the optimal vector from a predefined switching table in an intuitive way, are developed in [14] and [15] to replace the inner feedforward decoupling controller for reference tracking, but high power/torque ripple can be introduced into the system.

Considering its advantage of being able to reach a reference value with a fast dynamic response while satisfying a set of constraints, model predictive control (MPC) has been widely studied [16]. By making use of the inherent discrete nature of power converters, MPC evaluates the effect of each possible switching vector on the concerned variables in a predefined criterion and selects the optimal one that can minimize the differences between the concerned variables and their references. In [17], a long prediction horizon MPC is developed to control the back-to-back converter-fed PMSM system. Although the increased prediction horizon helps enhance the steady-state control performance, solving optimization problem is challenging and time consuming since the associated computational burden increases exponentially with the length of the prediction horizon. Thus, the finite control set MPC is the most widely applied [18]. Predictive direct power control is a widely applied method in

Manuscript received 12 June 2023; revised 12 October 2023 and 17 December 2023; accepted 2 January 2024. Date of publication 8 January 2024; date of current version 16 February 2024. This work was supported by the National Natural Science Funds of China under Grant 52277070. Recommended for publication by Associate Editor D. Zhang. *(Corresponding author: Xiaonan Gao.)*

Yingjie He, Ying Tang, Xiaonan Gao, Haotian Xie, and Ralph Kennel are with the Institute for Electrical Drive Systems and Power Electronics, Technical University of Munich, 80333 Munich, Germany (e-mail: yingjie.he@tum.de; ying.tang@tum.de; xiaonan.gao@tum.de; haotian.xie@fjirsm.ac.cn; ralph.kennel@tum.de).

Fengxiang Wang is with the National local joint Engineering Researching Center for Electrical Drive and Power Electronic, Quanzhou Institute of Equipment Manufacturing, Haixi Institutes, Chinese Academy of Sciences, Jinjiang 362200, China (e-mail: fengxiang.wang@fjirsm.ac.cn).

Color versions of one or more figures in this article are available at https://doi.org/10.1109/TPEL.2024.3350897.

Digital Object Identifier 10.1109/TPEL.2024.3350897

various drive systems. In [19], [20], and [21], it is adopted to control the rotor-side converter in the doubly fed induction generator drive system. In [22], instead of selecting a certain switching vector, the developed scheme adopts the switching time in addition to the switching vector to minimize the deviations from reference for the regulation of a three-level T-type inverter. Although an additional degree of freedom is enabled by choosing a variable switching point, the method complexity is also increased. In [23], a model predictive direct flux/power control is developed to reduce the computation burden by only evaluating the switching vectors selected from the newly designed switching tables. However, most MPCs in literature, including the references above, are adopted as an inner loop of the outer PI controller, which constructs the conventional PI controller-based model predictive control (PI-MPC). A dc-link voltage PI controller is always necessary to generate reference for MPC to control the back-to-back converter with PI-MPC [24]. This is a typical cascaded control structure because MPC is nesting inside the external voltage PI control loop [25], [26]. In order to further enhance the dynamic response of the system, a cascade-free method, which can remove the external dc voltage control loop, was developed in [27]. In this method, the power reference inside the cost function is directly obtained based on a power loss-less conversion assumption, i.e., the grid-side active power reference is computed by adding the desired load power and capacitor power. The calculated active power reference, which does not take the power converter losses, line losses, etc., into account, will be lower than the value it should be, which leads to a negative dc-link voltage bias. In addition, the voltage control performance is limited by the predefined number of intervals to reach the reference. If a faster tracking response on dc-link voltage is desired, a small value should be chosen for that number, but it will lead to large steady-state voltage ripple and large capacitor current. Zhang et al. [28] extended the above concept into a back-to-back converter by developing a quasi-centralized model predictive control (QC-MPC) scheme in which the active power reference inside the cost function is computed by assuming that the newly-updated voltage reference is reached at the next time instant. However, voltage tracking error still exists due to the adoption of the power loss-less model. To provide a solution for this problem, Zhang et al. [29] compensated for the voltage offset by adding the accumulated error into the active power reference in a revised QC-MPC. However, the response time of this scheme is subject to the reference prediction horizon. A small reference prediction horizon increases the dc-link currents and voltage fluctuation, but a large one prolongs the dynamic response time.

In this manuscript, a cascade-free control scheme is proposed for the back-to-back converter-fed PMSM system, and the main contributions are as follows.

1) *Achieve cascade-free control:* In PI-MPC, a dc-link voltage PI controller is always essential to produce power references for MPC in the back-to-back converter-fed PMSM drive system. It is a cascaded structure because the MPC is nesting inside the external voltage PI control loop. In this manuscript, a cascade-free MPC scheme without an additional voltage PI controller is proposed, which realizes the well-regulated dc-link voltage, controllable power flow, sine phase current, and near-unity power factor.
2) *Construct a new cost function:* A cost function integrating the dc-link voltage regulation term and power regulation term together is constructed, so that the control of dc-link voltage and power can be realized by a single cost function. During the cost function assessment, the switching vector, which is able to produce a smaller dc-link voltage error at the future time instant and is able to simultaneously produce an active power capable of further narrowing that voltage error, is chosen for the next time instant.
3) *Improve system robustness:* To predict accurately under variable parameters, the corrections for voltage and power expressions based on Luenberger observer are added to the proposed control scheme to remove the steady-state deviation even under the variable parameters, thus improving system robustness.

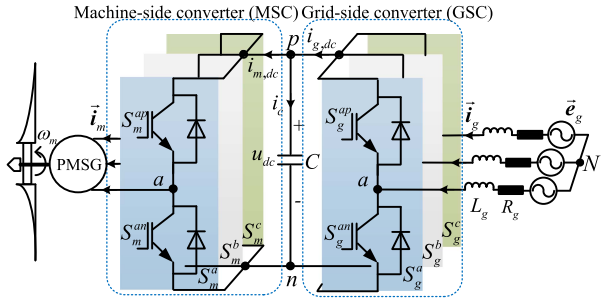

Fig. 1. Grid-connected PMSG system.

The rest of this article is organized as follows. First, the dynamic models of each part of the system are introduced in Section II. Then, the conventional PI-MPC, modified cascade-free QC-MPC schemes, and the proposed control scheme are presented in Section III. Afterward, experimental performance comparisons of the schemes are illustrated in Section IV. Finally, Section V concludes this article.

II. System Modelings and MPC Principle

In this section, the back-to-back converter-fed PMSM drive system illustrated in Fig. 1 is described in detail and the discrete expressions are given. The variables in abc stationary plane $\vec{\xi}_x^{abc}$, $x \in \{m, g\}$ (m denotes machine-side variables and g grid-side variables) can be mapped into $\alpha\beta$ stationary plane by the amplitude-invariant Clarke transformation matrix $\boldsymbol{M}_C$ and then mapped into dq rotating plane $\vec{\xi}_x^{dq} = [\xi_x^d, \xi_x^q]^{\mathrm{T}}$ by Park transformation matrix $\boldsymbol{M}_P$.

A. System Modelings

With the forward Euler discretization, the dynamic models of PMSM can be converted into the discrete models at time instant

$k+1$ as follows:

$$\begin{cases} \overrightarrow{\boldsymbol{i}}_m^{dq}[k+1] = \begin{bmatrix} 1-\frac{R_{m,s}T_s}{L_{m,s}} & w_{m,e}[k]T_s \\ -w_{m,e}[k]T_s & 1-\frac{R_{m,s}T_s}{L_{m,s}} \end{bmatrix} \overrightarrow{\boldsymbol{i}}_m^{dq}[k] \\ \quad + \frac{T_s}{L_{ms}} \boldsymbol{I}_2 \overrightarrow{\boldsymbol{u}}_m^{dq}[k] - \begin{pmatrix} 0 \\ \frac{T_s \psi_r}{L_{m,s}} w_{m,e}[k] \end{pmatrix} \\ \tau_{m,e}[k+1] = 1.5 n_p \psi_r i_m^q[k+1] \end{cases} \tag{1}$$

where $u_m, i_m, R_{m,s}, L_{m,s}, \psi_r, J_m, \tau_{m,e}, \tau_{m,m}, \omega_{m,m}, \omega_{m,e}$, n_p, and T_s denote the stator voltage, stator current, stator resistance, stator inductance, flux linkage, motor inertia, electromagnetic torque, load torque, mechanical angular speed, electrical angular speed, pole pairs of the generator, and sampling period, respectively, and $\boldsymbol{I}_2 = \mathrm{diag}(1,1)$. The stator voltage $\overrightarrow{\boldsymbol{u}}_m^{dq}$ can be regulated through configuring the power switches in MSC

$$\overrightarrow{\boldsymbol{u}}_m^{dq}[k] = \boldsymbol{M}_P \boldsymbol{M}_C \left(\overrightarrow{\boldsymbol{S}}_m^{\mathrm{abc}}[k] - \frac{1}{3} \sum_{y=a,b,c} S_m^y[k] \right) u_{\mathrm{dc}}[k] \tag{2}$$

where $\overrightarrow{\boldsymbol{S}}_m^{abc} = [S_m^a, S_m^b, S_m^c]^{\mathrm{T}}$, u_{dc} denotes the dc-link voltage, and $S_m^y, y \in \{a,b,c\}$ denotes the phase switching state of PMSM.

The discrete power models of GSC of time instant $k+1$ can be described as

$$\begin{cases} \begin{pmatrix} p_g[k+1] \\ q_g[k+1] \end{pmatrix} = \begin{bmatrix} 1-\frac{T_s R_g}{L_g} & -T_s \omega_g \\ \omega_g T_s & 1-\frac{T_s R_g}{L_g} \end{bmatrix} \begin{pmatrix} p_g[k] \\ q_g[k] \end{pmatrix} \\ \quad + \underbrace{\frac{3T_s}{2L_g} \begin{bmatrix} e_g^\alpha[k] & e_g^\beta[k] \\ e_g^\beta[k] & -e_g^\alpha[k] \end{bmatrix} \begin{pmatrix} e_g^\alpha[k] - u_g^\alpha[k] \\ e_g^\beta[k] - u_g^\beta[k] \end{pmatrix}}_{\Gamma[k]} \\ u_{\mathrm{dc}}[k+1] = u_{\mathrm{dc}}[k] + \frac{T_s}{C} \left\{ \left(\overrightarrow{\boldsymbol{S}}_g^{abc}[k] \right)^{\mathrm{T}} \overrightarrow{\boldsymbol{i}}_g^{abc}[k] \right. \\ \quad \left. - \left(\boldsymbol{S}_m^{abc}[k] \right)^{\mathrm{T}} \overrightarrow{\boldsymbol{i}}_m^{abc}[k] \right\} \end{cases} \tag{3}$$

where $e_g, u_g, i_g, R_g, L_g, p_g, q_g$, and C are grid-side voltage, converter voltage, grid-side current, filter resistance, filter inductance, active power, reactive power, and capacitance of dc-link capacitor, respectively. The converter voltage $\overrightarrow{\boldsymbol{u}}_g^{\alpha\beta}$ can be regulated through configuring the power switches in GSC

$$\overrightarrow{\boldsymbol{u}}_g^{\alpha\beta}[k] = \boldsymbol{M}_C \left(\overrightarrow{\boldsymbol{S}}_g^{abc} \left([k] - \frac{1}{3} \sum_{y=a,b,c} S_g^y[k] \right) u_{\mathrm{dc}}[k] \right. \tag{4}$$

where $\overrightarrow{\boldsymbol{S}}_g^{abc} = [S_g^a, S_g^b, S_g^c]^{\mathrm{T}}$, and S_g^y denotes the phase switching state of GSC. Shifting forward one T_s on (1) and (3) obtains the discrete models at time instant $k+2$.

B. MPC Principle

In MPC, the effect of each possible converter switching vector on the concerned variables is calculated according to the predictive model, and the optimal one, i.e., $\vec{\boldsymbol{S}}_x^{\mathrm{opt}}[k]$, selected during $[k, k+1]$ should be applied during the entire time interval of $[k, k+1]$ in an ideal case. However, in a practical system, the time delay in digital implementation makes $\vec{\boldsymbol{S}}_x^{\mathrm{opt}}[k]$ cannot be implemented to power switches at time instant k in time [30]. To address this problem, time delay compensation is considered in MPC so that the optimal switching vector $\vec{\boldsymbol{S}}_x^{\mathrm{opt}}[k]$ for interval $[k, k+1]$ can be got during interval $[k-1, k]$ and applied at time instant k. The cost function $J_x, x \in \{m, g\}$ with time delay compensation is defined as

$$\begin{cases} J_x \left(\boldsymbol{S}_x^{\mathrm{opt}}[k+1] \right) = \min_{\boldsymbol{S}_x^{\mathrm{abc}} \in V_x} J_x \left(\boldsymbol{S}_x^{\mathrm{abc}}[k+1] \right) \\ J_x \left(\overrightarrow{\boldsymbol{S}}_x^{\mathrm{abc}}[k+1] \right) = \lambda_f \left\| F_x^* - f_x[k+2] \right\|^2 + \zeta_x \end{cases} \tag{5}$$

where $f_x[k+2]$ denotes concerned variables predicted based on the possible switching vector $\overrightarrow{\boldsymbol{S}}_x^{\mathrm{abc}}[k+1]$ of time instant $k+1$, $\vec{\boldsymbol{S}}_x^{\mathrm{opt}}[k+1]$ denotes the optimal switching vector of time instant $k+1$, F_x^* denotes the references of the concemed variables, and ζ_x represents the system constraint. According to their nature, the terms in the cost function can be sorted into different groups to facilitate the adjustment procedure of weighting factors λ_f, and the branch and bound method illustrated in [31] is commonly used to tune λ_f in various cost functions (the cost function with equally important terms, the cost function with secondary term, etc.). Constraint ζ_x is introduced into the cost function to limit the concerned system variables within a safe range, and it is given by

$$\zeta_x = \begin{cases} 0, \text{ if } \left\| h_x \left(\overrightarrow{\boldsymbol{S}}_x^{\mathrm{abc}}[k+1] \right) \right\| \le \| h_x^{\max} \| \\ \infty, \text{ if } \left\| h_x \left(\overrightarrow{\boldsymbol{S}}_x^{\mathrm{abc}}[k+1] \right) \right\| > \| h_x^{\max} \| \end{cases} \tag{6}$$

where h_x and $h_x^{\max}$ denote the mathematical expression and maximum of the concerned system variables, respectively. The following cost function is adopted for the selection of the optimal switching vector for MSC:

$$\begin{aligned} & J_m \left(\overrightarrow{\boldsymbol{S}}_m^{\mathrm{abc}}[k+1] \right) \\ & = \lambda_T \left\| \tau_{m,e}^* - \tau_{m,e}[k+2] \right\|^2 + \left\| i_m^{d\,*} - i_m^d[k+2] \right\|^2 \\ & \quad + \underbrace{\begin{cases} 0, & \text{if } \| \tau_{m,e}[k+2] \| \le \left\| \tau_{m,e}^{\max} \right\| \\ \infty, & \text{if } \| \tau_{m,e}[k+2] \| > \left\| \tau_{m,e}^{\max} \right\| \end{cases}}_{\zeta_{m,\tau_{me}}} \\ & \quad + \underbrace{\begin{cases} 0, & \text{if } \left\| \overrightarrow{\boldsymbol{i}}_m^{dq}[k+2] \right\| \le \| i_m^{\max} \| \\ \infty, & \text{if } \left\| \overrightarrow{\boldsymbol{i}}_m^{dq}[k+2] \right\| > \| i_m^{\max} \| \end{cases}}_{\zeta_{m,i_{dq}}} \end{aligned} \tag{7}$$

where $\zeta_{m,\tau_{me}}$ and $\zeta_{m,i_{dq}}$ denote the constraints for torque and current limitation, respectively.

III. Conventional and Proposed Cascade-Free Control Schemes

A. Modified QC-MPC Schemes

For conventional PI-MPC, a dc-link voltage PI controller is always necessary for the regulation of back-to-back converter [24], [28]. The control structure is cascaded, as the inner MPC is nesting inside the outer voltage PI control loop.

Without outer dc-link voltage PI control loop, the QC-MPC scheme achieves voltage regulation according to the dynamic reference generation concept [27]. In this concept, the dc-link voltage set point $u^*_{\mathrm{dc},\infty}$ is not fully given to the controller at one time, and a reference prediction horizon N_s is adopted to specify the actual dc-link voltage reference of each time instant u^*_{dc}[28]

$$u^*_{\mathrm{dc}} = u_{\mathrm{dc}}[k] + \frac{1}{N_s}\left(u^*_{\mathrm{dc},\infty} - u_{\mathrm{dc}}[k]\right). \tag{8}$$

To reach u^*_{dc} at the next time instant, the grid-side active power reference p^*_g can be estimated by [29]

$$p^*_g = \frac{3\left(e^d_g\right)^2}{4R_g} - \sqrt{\frac{9\left(e^d_g\right)^4}{16R_g^2} - \frac{3\left(e^d_g\right)^2}{2R_g}p^*_{g,\mathrm{dc}}} \tag{9}$$

where $p_{g,\mathrm{dc}}$ denotes instantaneous power of the MSC and dc-link capacitor, and e^d_g denotes the d-axis component of grid-side voltage. Then, $\overrightarrow{\boldsymbol{S}}^{\mathrm{opt}}_g[k+1]$ can be selected by evaluating

$$\begin{aligned} &J_{g,\mathrm{QC}}\left(\boldsymbol{S}^{\mathrm{abc}}_g[k+1]\right) \\ &= \underbrace{\left\|p^*_g - p_g[k+2]\right\|^2}_{F_{g,p}} + \underbrace{\lambda_q\left\|q^*_g - q_g[k+2]\right\|^2}_{F_{g.q}} \\ &\quad + \underbrace{\lambda_{u\mathrm{dc}}\left\|u^*_{\mathrm{dc}} - u_{\mathrm{dc}}[k+2]\right\|^2}_{F_{g,u}} \\ &\quad + \underbrace{\begin{cases} 0, & \text{if } \left\|\vec{\boldsymbol{S}}_g[k+2]\right\| \le \left\|s^{\max}_g\right\| \\ \infty, & \text{if } \left\|\vec{\boldsymbol{S}}_g[k+2]\right\| > \left\|s^{\max}_g\right\| \end{cases}}_{\zeta_a} \end{aligned} \tag{10}$$

where $\vec{s}_g = [p_g, q_g]^{\mathrm{T}}$ and q^*_g denotes the grid-side reactive power references.

In this QC-MPC scheme, the dc-link voltage tracking performance heavily depends on N_s, and N_s serves as a tradeoff between response time in dynamics against dc-link voltage ripple in steady state [27]. To improve the dynamic performance of the QC-MPC, a modified QC-MPC is proposed. In the proposed modified QC-MPC, a dynamic reference prediction horizon is adopted for (8) to compute the actual dc-link voltage reference of each time instant

$$N_s = N_{s,\mathrm{st}} - c_{Te}\left\|u^*_{\mathrm{dc},\infty} - u_{\mathrm{dc}}[k]\right\| \tag{11}$$

where $N_{s,\mathrm{st}}$ represents the reference prediction horizon used in steady state, and $c_{\mathrm{re}} \in \mathrm{R}_+$represents the regulation coefficient. It aims to reduce the dynamic response time by reducing N_s while achieving a satisfying steady-state dc-link voltage control performance. However, tracking dc-link voltage set point by strictly specifying the actual reference for each time instant is still the core of QC-MPC.

B. Proposed Cascade-Free Control Scheme

Ideally, actual inductance and resistance (L_g and R_g), should be used in the discrete power expression in (3) for prediction to get an accurate result. However, it is a condition that cannot be met easily in reality. In the practical system, it is the nominal inductance and resistance ($L_{g,n}$ and $R_{g,n}$) that are used for prediction, and the actual inductance and resistance will change in different operating conditions, which results in steady-state deviations in power. In addition, since the voltage expression in (3) ignores the equivalent resistances of semiconductors and diodes, it is a rough prediction and the steady-state deviation on dc-link voltage will be produced if it is directly used for voltage prediction.

Luenberger observer not only can be used to enhance the robustness of the system against mismatched parameters but can be used to improve the performance affected by measurement noise. To eliminate the steady-state deviations on power, the uncertainties caused by parameter variations are regarded as dynamic disturbances, then the power expression of (3) can be rewritten as

$$\begin{aligned} \begin{pmatrix} p_g[k+1] \\ q_g[k+1] \end{pmatrix} &= \begin{bmatrix} 1 - \frac{T_s R_{g,n}}{L_{g,n}} & -T_s\omega_g \\ \omega_g T_s & 1 - \frac{T_s R_{g,n}}{L_{g,n}} \end{bmatrix} \begin{pmatrix} p_g[k] \\ q_g[k] \end{pmatrix} \\ &\quad + \frac{3T_s}{2L_{g,n}}\boldsymbol{\Gamma}[k] - \frac{T_s}{L_{g,n}}\begin{pmatrix} \delta_{g,p}[k] \\ \delta_{g,q}[k] \end{pmatrix} \end{aligned} \tag{12}$$

where $\delta_{g,p}$ and $\delta_{g,q}$ are the disturbances in active power and reactive power expression, respectively. The grid-side input power is the sum of the power of PMSM and dc-link capacitor in an ideal case because of the power balance

$$u_{\mathrm{dc}}(t)C\frac{du_{\mathrm{dc}}(t)}{dt} = \frac{C}{2}\frac{du^2_{\mathrm{dc}}(t)}{dt} = p_g(t) - \tau^*_{m,c}\omega_{m,m}(t). \tag{13}$$

Since power converter loss, line loss, etc., in the realistic case are not considered in (13), steady-state deviation on dc-link voltage will be generated if it is used for voltage prediction. To predict accurately, the unconsidered power converter loss is regarded as a disturbances $\delta_{u\mathrm{dc}}$, then the discrete form of (13) can be modified into

$$u^2_{\mathrm{dc}}[k+1] = \frac{2T_s}{C}\left(p_g[k] - \tau^*_{m,c}\omega_{m,m}[k] + \delta_{u\mathrm{dc}}[k]\right) + u^2_{\mathrm{dc}}[k]. \tag{14}$$

After combining (12) and (14), the system state-space equation can be obtained as follows:

$$\begin{aligned} \boldsymbol{\Lambda}[k+1] &= \underbrace{\begin{bmatrix} \boldsymbol{E} & \boldsymbol{H} \\ \boldsymbol{0}_{3\times 3} & \boldsymbol{I}_3 \end{bmatrix}}_{M_A}\boldsymbol{\Lambda}[k] \\ &\quad + \frac{3T_s}{2L_{g,n}}\underbrace{\begin{bmatrix} \boldsymbol{Z}[k] \\ \boldsymbol{0}_{3\times 3} \end{bmatrix}}_{\boldsymbol{M}_B[\mathrm{k}]}\begin{pmatrix} e^\alpha_g[k] - u^\alpha_g[k] \\ e^\beta_g[k] - u^\beta_g[k] \\ \tau^*_{m,c^*}\omega_{m,m}[k] \end{pmatrix} \end{aligned} \tag{15}$$

where

$$\boldsymbol{\Lambda} = (p_g, q_g, u^2_{dc}, \delta_{g,p}, \delta_{g,q}, \delta_{u\mathrm{dc}})^{\mathrm{T}}$$

$$\boldsymbol{H} = \begin{bmatrix} -\frac{T_s}{L_{g,n}} & 0 & 0 \\ 0 & -\frac{T_s}{L_{g,n}} & 0 \\ 0 & 0 & \frac{2T_s}{C} \end{bmatrix}$$

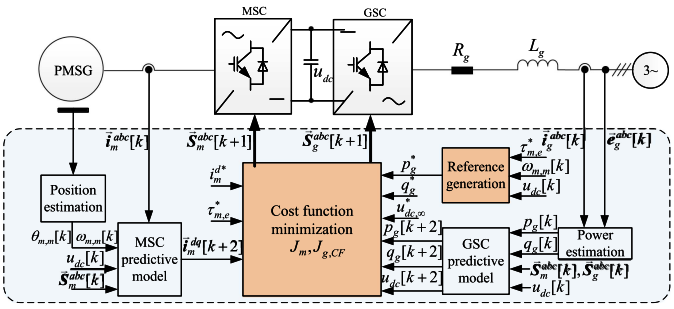

Fig. 2. Control structure of the proposed cascade-free control scheme.

$$\boldsymbol{E} = \begin{bmatrix} 1 - \frac{T_s R_{g,n}}{L_{g,n}} & -T_s\omega_g & 0 \\ T_s\omega_g & 1 - \frac{T_s R_{g,n}}{L_{g,n}} & 0 \\ \frac{2T_s}{C} & 0 & 1 \end{bmatrix}$$

$$\boldsymbol{Z}[k] = \begin{bmatrix} e_g^{\alpha}[k] & e_g^{\beta}[k] & 0 \\ e_g^{\beta}[k] & -e_g^{\alpha}[k] & 0 \\ 0 & 0 & -\frac{4L_{g,n}}{3C} \end{bmatrix}.$$

Then, the state-space equation based on Luenberger observer, which is used to remove the voltage and power deviations under variable parameter, can be obtained as follows:

$$\hat{\boldsymbol{\Lambda}}[k+1] = \boldsymbol{M}_A\hat{\boldsymbol{\Lambda}}[k] + \frac{3T_s}{2L_{g,n}}\boldsymbol{M}_B[k]\begin{pmatrix} e_g^{\alpha}[k] - u_g^{\alpha}[k] \\ e_g^{\beta}[k] - u_g^{\beta}[k] \\ \tau_{m,e}^{*}\omega_{m,m}[k] \end{pmatrix} + \boldsymbol{M}_L(\boldsymbol{X}[k] - \widehat{\boldsymbol{X}}[k]) \tag{16}$$

where $\boldsymbol{X} = (p_g, q_g, u_{dx}^2, p_g, q_p, u_{d2}^2)^{\mathrm{T}}$, $\widehat{\boldsymbol{X}}$ represents the estimated variable of $\boldsymbol{X}$, the coefficient diagonal matrix M_L can be determined by the pole placement method [30], and $\hat{\boldsymbol{A}}$ represents the estimated variable of $\boldsymbol{A}$. Then, the obtained $\hat{\delta}_{g,p}$, $\hat{\delta}_{g,q}$, and $\hat{\delta}_{u\mathrm{dc}}$ can be used to correct the prediction model. The following term is used for dc-link voltage regulation:

$$F_{g,u}\left(\vec{\boldsymbol{S}}_g^{\mathrm{abc}}[k+1]\right) = \underbrace{\left\|u_{\mathrm{dc},\infty}^{*} - u_{\mathrm{dc}}[k+2]\right\|^2}_{E_{g,u}} + \underbrace{\left\|\left(u_{\mathrm{dc},\infty}^{*\,2} - u_{\mathrm{dc}}^2[k+2]\right) + c_p\left(p_g^{*} - p_g[k+2]\right)\right\|^2}_{R_{g,u}} \tag{17}$$

where $R_{g,u}$ and $E_{g,u}$ are used to control dc-link voltage and active power of time instant $k+2$, $c_p \in \mathrm{R}_+$is for active power regulation, and p_g^{*} is the power of PMSM, namely $\tau_{m,c}^{*}\omega_{m,m}[k]$. Then, the cost function of the proposed control scheme is defined as

$$J_{g,\mathrm{CF}}\left(\vec{\boldsymbol{S}}_g^{\mathrm{abc}}[k+1]\right) = F_{g,u} + F_{g,q} + \zeta_s. \tag{18}$$

The control structure of the proposed cascade-free control scheme is presented in Fig. 2.

Since the terms in the cost function can be controlled by MPC to approach zero to realize the reference track, assume that $R_{g,u}$ and $E_{g,u}$ in (17) are equal to zero in the interpretation below. Besides, the generator mode of PMSM corresponding to a negative p_g^{*} is taken as an example for description. In the proposed control scheme, the voltage set point $u_{\mathrm{dc},\infty}^{*}$ is directly adopted in $E_{g,u}$ as the reference to compare with the dc-link voltage produced by every switching vector at time instant $k+2$, so the switching vector that leads to the smaller dc-link voltage error tends to be chosen. If a switching vector will produce a dc-link voltage smaller than its reference $u_{\mathrm{dc},\infty}^{*}$ at time instant $k+2$ in $E_{g,u}$, this switching vector is the optimal one only when it also will transmit less power back to the grid than the produced PMSM power due to $R_{g,w}$. It means if ${u_{\mathrm{dc},\infty}^{*}}^2 > u_{\mathrm{dc}}^2[k+2]$ for a switching vector, not all the power produced by PMSM should be transmitted to grid by that switching vector (i.e., $p_g^{*} < p_g[k+2]$). In this way, the dc-link capacitor can be charged by the remained power produced by PMSM, thereby reducing the voltage error. When $u_{\mathrm{dc}}[k+2]$ reaches $u_{\mathrm{dc},\infty}^{*}$, $p_g[k+2]$ equals p_g^{*}, which means all the power produced by PMSM is transmitted to the grid in steady state. As can be found above, the switching vector, which is able to produce a dc-link voltage closer to the reference and is able to simultaneously produce an active power capable of further narrowing that voltage error, is chosen for the next time instant.

C. Stability Analysis

According to Kirchhoff's voltage law, the following state equations can be obtained (the models are eventually derived in discrete-time format by applying the forward Euler method of $\frac{d}{dt}x(t) = \frac{x[k+1]-x[k]}{T_s}$):

$$\boldsymbol{x}_y[k+1] = \boldsymbol{A}_y[k] - \boldsymbol{x}_y[k] + \boldsymbol{B}_y[k]\cdot\boldsymbol{u}_y[k] + \boldsymbol{H}_y[k] \tag{19}$$

where $y \in \{m, g\}$ represents the variables of machine (m) and grid (g) sides, respectively.

It can be seen that the inductance is involved in the state, input, and feed-through matrices, i.e., $\boldsymbol{A}_y[k]$, $\boldsymbol{B}_y[k]$, and $\boldsymbol{H}_y[k]$. The nominal inductance used in the controller is denoted as $\tilde{L}_y$ while the actual inductance value is denoted as L_y. The predicted value of the state variables based on the nominal value can be obtained as

$$\boldsymbol{x}_y^p[k+1] = \tilde{\boldsymbol{A}}_y[k]\cdot\boldsymbol{x}_y[k] + \widetilde{\boldsymbol{B}}_y[k]\cdot\boldsymbol{u}_y^p[k] + \tilde{\boldsymbol{H}}_y[k] \tag{20}$$

where $\boldsymbol{x}_y^p$ and $\boldsymbol{u}_y^p$ stand for predicted values of the state and input variables, respectively. As the control period of the current loop is 50 μs, both the inductance and resistance in the system are small enough to ignore. Thus, the system matrix $\tilde{\boldsymbol{A}}_y$ used here is simplified as $\boldsymbol{I}_2 = \mathrm{diag}(1,1)$. Then, the input voltage vectors $u^p[k]$ can be calculated by

$$\boldsymbol{u}_y^p[k] = \widetilde{\boldsymbol{B}}_y[k]^{-1}\left(\boldsymbol{x}_y^p[k+1] - \tilde{\boldsymbol{H}}_y[k] - \tilde{\boldsymbol{A}}_y[k]\cdot\boldsymbol{x}_y[k]\right). \tag{21}$$

Applying (21) into (19) gives

$$\boldsymbol{x}_y^m[k+1] = \boldsymbol{A}_y[k]\cdot\boldsymbol{x}_y^m[k] + \boldsymbol{M}[k]\left(\boldsymbol{x}_y^p[k+1] - \tilde{\boldsymbol{H}}_y[k] - \tilde{\boldsymbol{A}}_y[k]\cdot\boldsymbol{x}_y^m[k]\right) + \boldsymbol{H}_y[k] \tag{22}$$

where x_y^m stand for measured values of state variables, and $\boldsymbol{M}[k] = \boldsymbol{B}_y[k] - \widetilde{\boldsymbol{B}}_y[k]^{-1}$. Since $\boldsymbol{x}_y^p[k+1]$ will approach

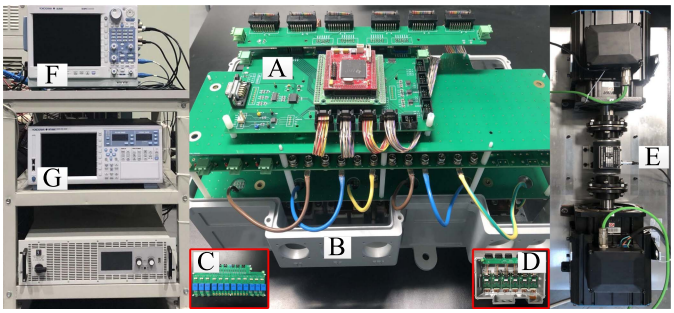

Fig. 3. Laboratory setup. (a) TMS320F28335-based control board. (b) GSC and MSC. (c) Voltage and current transducers. (d) Power modules. (e) PMSM and its load motor. (f) Yokogawa DL850. (g) Yokogawa WT1800.

$x_y^*[k+1]$, so the following expression holds:

$$\boldsymbol{x}_y^m[k+1] = \frac{\vec{L}_y}{L_y}\boldsymbol{x}_y^*[k+1] + \left(1 - \frac{\tilde{L}_y}{L_y}\right)\boldsymbol{x}_y^m[k]. \tag{23}$$

The closed-loop transfer function in discrete format becomes

$$\frac{x_y^m(z)}{x_y^*(z)} = \frac{\frac{\bar{L}_y}{L_y}z}{z - 1 + \frac{\tilde{L}_v}{L_v}}. \tag{24}$$

Based on the "bounded-input bounded-output" stability criteria from the classic control theory, the system in this work is stable if and only if all roots of $F(z) = z - 1 + \frac{\tau_y}{L_y}$ are inside the unit circle [32]. Thus, when $\vec{L}_y \in (0, 2L_y)$, the system will be stable.

$$|z| = \left|1 - \frac{\tilde{L}_v}{L_v}\right| < 1. \tag{25}$$

IV. Experimental Evaluation

The proposed cascade-free control scheme is evaluated on a practical laboratory setup shown in Fig. 3, and its experimental comparisons with PI-MPC, modified QC-MPC, and PI control scheme with modulator are presented. The scheme calculation time of PI-MPC, modified QC-MPC, proposed control scheme, and PI control with modulator are 14.7, 14.1, 15.4, and 14.4 μs, respectively. It can be found that the control schemes consume similar calculation time in the microcontroller. The calculation time of around 15 μs indicates the time of the core code control program, namely, the duration related to how to calculate their respective switching vector in different control schemes. The core code is the main difference between different control methods, but for the whole interrupt, it takes around 43 μs for each control scheme to complete a whole interrupt. Table I lists the hardware configurations of several main components in the laboratory setup. The experimental parameters concerning the MSC, GSC, and control data are itemized in Table II.

The experimental results of the proposed cascade-free control scheme at the rated speed of 1500 r/min are presented in Fig. 4 to show the steady-state regulation performance. For the PMSM side, the electromagnetic torque is set to $-12\,\mathrm{N}\cdot\mathrm{m}$ (the yellow dash on the upper left of the torque curve denotes $0\,\mathrm{N}\cdot\mathrm{m}$), and the sinusoidal stator current of around 4.3 A (rms value)

TABLE I
Hardware Configurations of Main Components

Hardware	Manufacturer	Type
DSP	TI	TMS320F28335
IGBT module	INFINEON	FF300R12ME4
Current transducer	LEM	LA25
Voltage transducer	LEM	LV25
Incremental encoder	HEIDENHAIN	ERO1420

TABLE II
Experimental System Parameters

Description	Parameter	Value	Description	Parameter	Value
GC			PMSG		
Voltage Frequency	ω_g (rad/s)	100π	Pole pairs	n_p	4
Filter resistance	R_g (Ω)	0.1	Permanent-magnet flux linkage	ψ_r (Wb)	0.388
Filter inductor	L_g (mH)	12	Stator inductor	$L_{m,s}$ (mH)	11.7
Phase voltage	e_g (V)	180	Stator resistance	$R_{m,s}$ (Ω)	0.985
DC-link capacitor	C (μF)	100	Rated torque	$\tau_{m,e}$ $(N\cdot m)$	12
Control period	T_s (μs)	50	Rated speed	$n_{m,e}$ (r/min)	1500

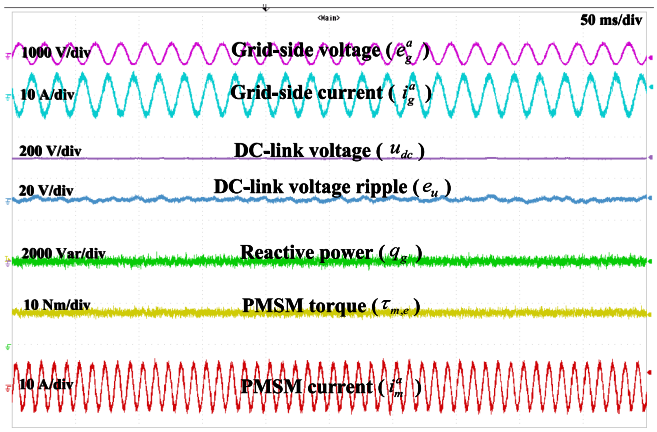

Fig. 4. Experimental results of the proposed control scheme at rated operating condition (1500 r/min, $-12\,\mathrm{N}\cdot\mathrm{m}$).

is obtained to reach the reference torque. For the grid side, the energy produced by PMSM has been continuously transmitted into the grid to keep a stable dc-link voltage under the proposed scheme. The dc-link voltage has been boosted to 500 V, and the difference between the actual and reference dc-link voltage (i.e., $e_u = u_{\mathrm{dc}} - u_{\mathrm{dc},\infty}^*$) is defined to evaluate the regulation quality of dc-link voltage, and it is observed that the dc-link voltage ripple has been regulated within ± 3 V. In this process, the sinusoidal grid-side current in the opposite phase with the grid-side voltage is obtained because the reactive power has been kept around 0 Var. The switching frequency of the finite control set-model predictive control (FCS-MPC) is almost fixed in a steady state. In the system with the proposed control scheme, the equivalent switching frequency is around 3 kHz at the rated operating condition.

The dynamic performances of PI-MPC, modified QC-MPC, and the proposed cascade-free control scheme in different operating conditions are tested and compared. Besides, for a better comparison, the dynamic performances of PI control scheme with modulator are also added, and its switching frequency is set to be the same (3 kHz) as that of the proposed control scheme. In the implementation of the aforementioned four schemes, the grid-side voltage, grid-side inductor, dc-link capacitor, operating state of PMSM, semiconductors, etc., are kept the same.

The experimental results under abrupt torque change at rated speed are shown in Fig. 5. The dc-link voltage increases at the moment when torque decreases from 12 to $-12\,\mathrm{N}\cdot\mathrm{m}$ since PMSM suddenly starts to produce power instead of consuming power. Although the direction of active power flow is reversed under these abrupt torque changes, the dc-link voltage can be pulled back to its reference by transmitting the active power to the grid in time under the controls of the four schemes. As can be seen from the curves, the peak errors of dc-link voltage e_u are $20, 18, 12$, and $22\,\mathrm{V}$ for PI-MPC, modified QCMPC, proposed scheme, and PI scheme with modulator, respectively, and the recovery times of dc-link voltage are around $200, 100, 50$, and $300\,\mathrm{ms}$, respectively. The proposed scheme has a better dynamic regulation performance compared with the other three schemes since it presents the smaller peak error and faster recovery time.

The experimental results under abrupt reactive power changes at the rated operating state are presented in Fig. 6. The change of grid-side reactive power reference from -1000 to 1000 Var affects the dc-link voltage due to the coupling between reactive power and active power. The dc-link voltage in the proposed control scheme presents a smaller decrease of -3 V, in comparison with -5 V of the modified QC-MPC, -6.5 V of the PI-MPC, and -7 V of the PI scheme with modulator. Since the dc-link voltage in the proposed control scheme is least affected, it is also the fastest to return back to the reference. The recovery times of dc-link voltage in the proposed control scheme, modified QC-MPC, PI-MPC, and PI scheme with modulator are around 20, 50, 200, and 350 ms, respectively.

Experimental results under abrupt speed changes are presented in Fig. 7. At $-12\ \mathrm{N}\cdot\mathrm{m}$, the operating status of the PMSM changes from generating mode to motoring mode as the speed changes from 1500 to -1500 r/min. Correspondingly, the phase of grid-side current changes from being in the opposite direction to being in the same direction as the grid-side voltage. It indicates that the operating status of GSC is changed from transmitting power in the machine-to-grid direction to providing power in the grid-to-machine direction to keep a constant dc-link voltage. Speed, unlike electromagnetic torque, is a mechanical parameter, so the change of speed direction results in a slower operating change for the system, which gives the control schemes more time to respond. It can be seen from the curves that the modified QC-MPC and the proposed control scheme present satisfying dc-link voltage regulation performance since both of them are hardly affected during this regulation. But, compared with modified QC-MPC, the proposed control scheme has a slightly smaller voltage peak error during this dynamic regulation, and both of their peak errors are smaller than that of the PI-MPC and PI scheme with modulator. The peak errors

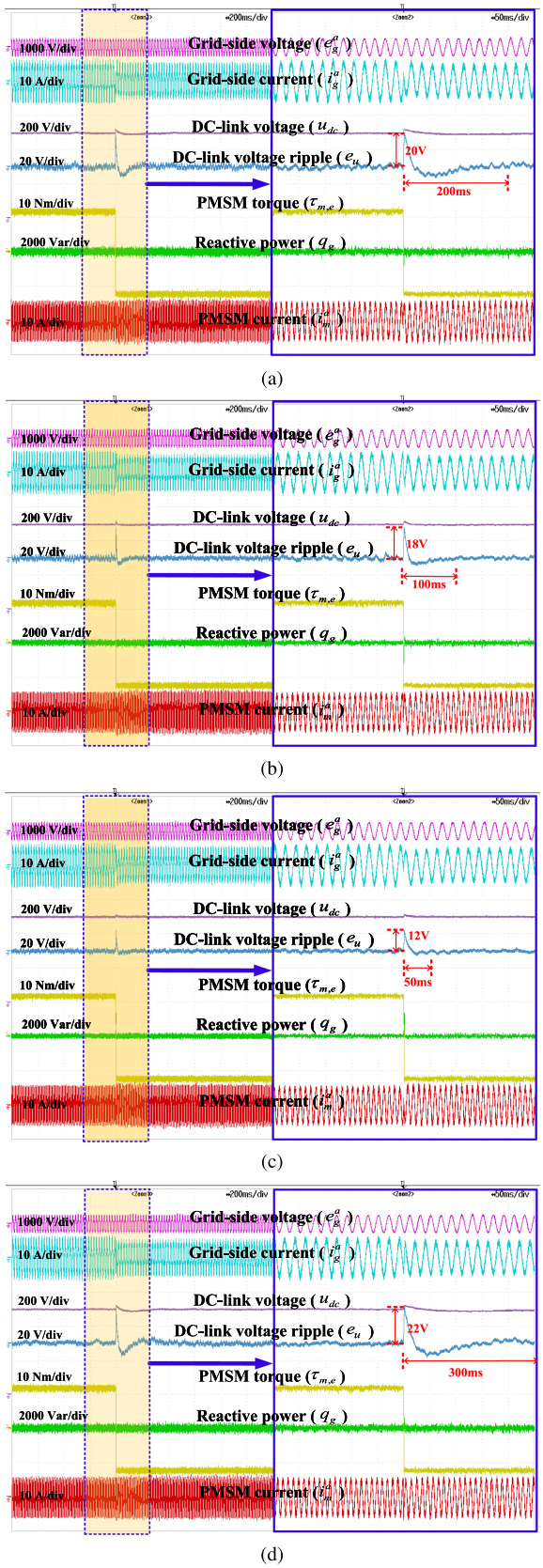

Fig. 5. Experimental results under abrupt torque change (from 12 to $-12\ \mathrm{N}\cdot\mathrm{m}$) at rated speed. (a) PI-MPC. (b) Modified QC-MPC. (c) Proposed control scheme. (d) PI control scheme with modulator.

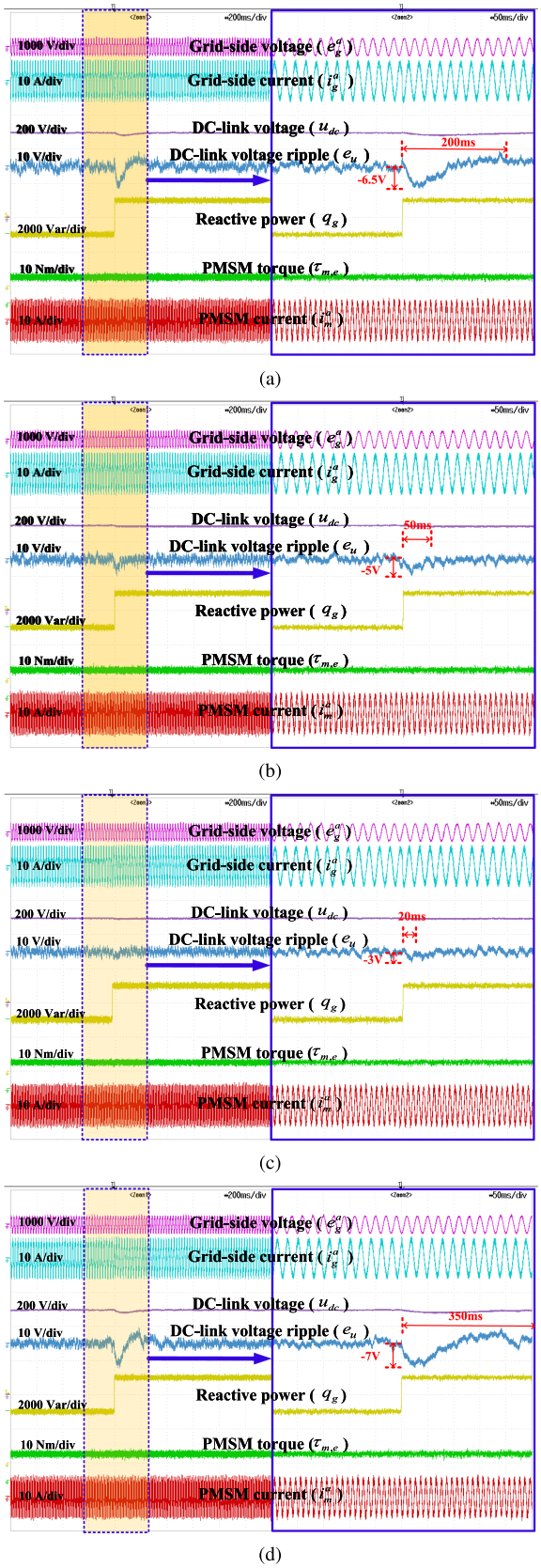

Fig. 6. Experimental results under abrupt reactive power changes (from −1000 to 1000 Var) at rated speed. (a) PI-MPC. (b) Modified QC-MPC. (c) Proposed control scheme. (d) PI control scheme with modulator.

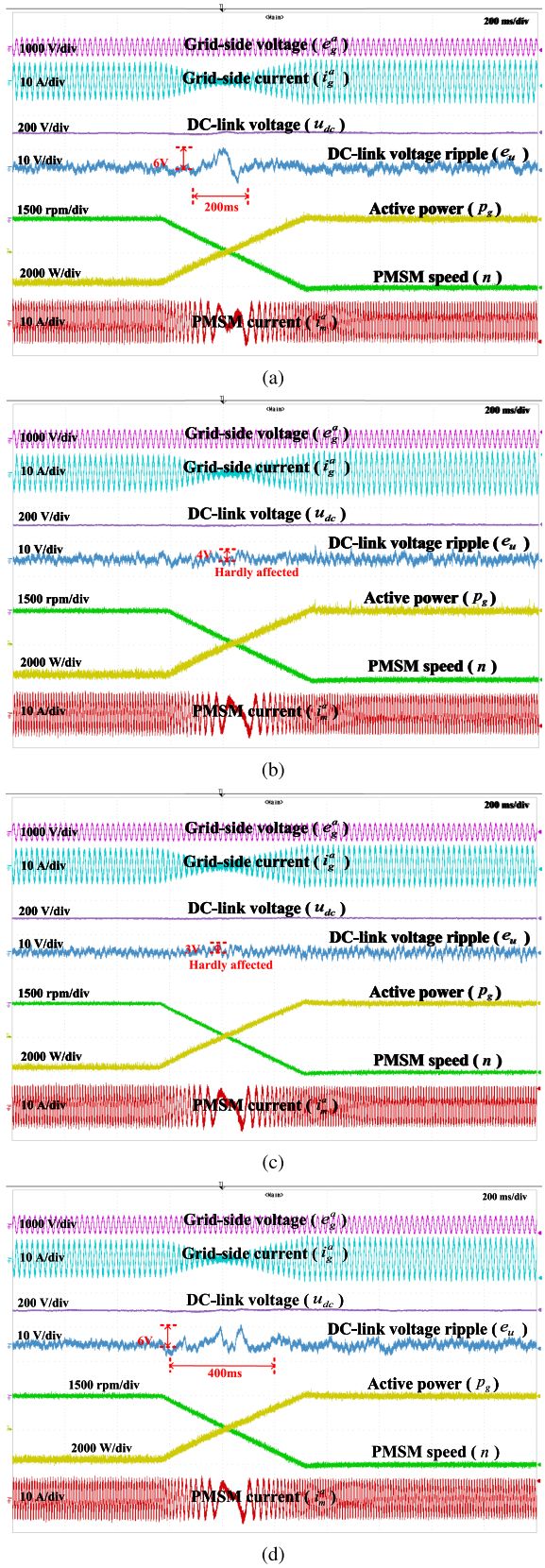

Fig. 7. Experimental results under abrupt speed changes (from 1500 to −1500 r/min) at −12 N · m. (a) PI-MPC. (b) Modified QC-MPC. (c) Proposed control scheme. (d) PI control scheme with modulator.

TABLE III
COMPARISON DATA UNDER VARIOUS TEST CONDITIONS

Test conditions	Control schemes	Peak errors of DC-link voltage (V)	Recovery time (ms)
Abrupt torque change from 12 to -12 N · m	PI-MPC	20	200
	Modified QC-MPC	18	100
	Proposed control scheme	12	50
	PI control with modulator	22	300
Abrupt reactive power changes from -1000 to 1000 Var	PI-MPC	-6.5	200
	Modified QC-MPC	-5	50
	Proposed control scheme	-3	20
	PI control with modulator	-7	350
Abrupt speed changes from 1500 to -1500 r/min	PI-MPC	6	200
	Modified QC-MPC	4	Hardly affected
	Proposed control scheme	3	Hardly affected
	PI control with modulator	6	400

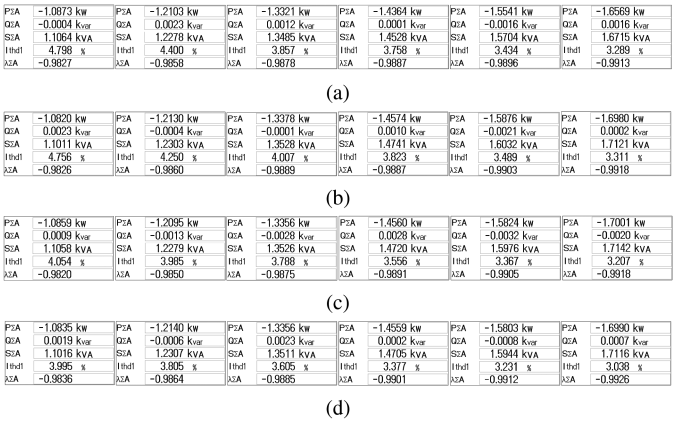

Fig. 8. Power analyzer screenshots at different speeds (from left-hand side to right-hand side: 1000, 1100, 1200, 1300, 1400, and 1500 r/min). (a) PI-MPC. (b) Modified QC-MPC. (c) Proposed control scheme. (d) PI control scheme with modulator.

of dc-link voltage are around 6, 4, 3, and 6 V for PI-MPC, modified QC-MPC, proposed control scheme, and PI scheme with modulator, respectively.

The experimental data of PI-MPC, modified QC-MPC, proposed control scheme, and PI control scheme with modulator in the aforementioned dynamic tests, which reflects their transient performances, are summarized in Table III. It can be found that the dynamic regulation performances of all three MPC-based control schemes (PI-MPC, modified QC-MPC, and proposed control scheme) are obviously better than that of the PI control scheme with modulator. Furthermore, compared with the other two MPC-based control schemes, the proposed control scheme presents a faster dynamic response during the transients of the abrupt changes of torque, reactive power, and speed since it presents smaller peak errors and shorter recovery time.

The experimental data of the four control schemes from the power analyzer screenshots (Yokogawa WT1800E), which reflect their steady-state performances at different operating speeds, are presented in Fig. 8. As can be seen from the current total harmonic distortions (THDs) (Ithd_1) and power factors ($\lambda \sum A$) in Fig. 8, the PI scheme with modulator has a slightly better steady-state regulation performance than the three MPC-based schemes at the same switching frequency,

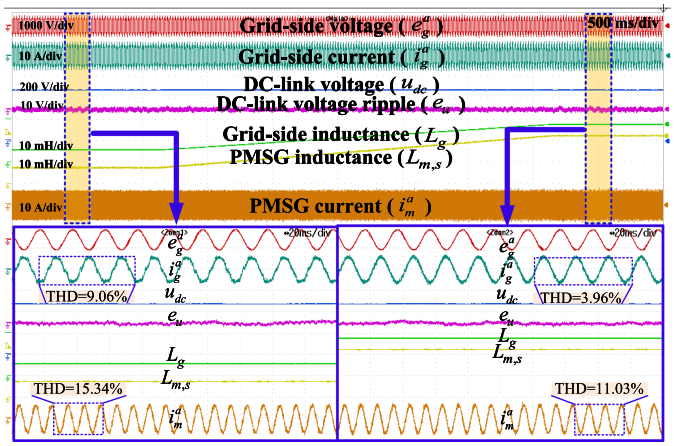

Fig. 9. Experimental waveforms of proposed control strategy under mismatched inductances.

but it has the slowest regulation performance in transients (as presented in Table I). However, the steady-state performances of the MPC-based schemes are comparable to that of the PI scheme with modulator since the MPC-based schemes can also control the current THDs below 3.5% and keep the grid-side power factors above 0.99 at the rated operating condition.

Considering that the model accuracy is more affected by the changes in inductance than resistance, the case of mismatched inductances is adopted to test the control performance of the proposed control scheme, and experimental results are presented in Fig. 9. Without the disturbance estimation, steady-state deviations would appear on the power curves when there is a difference between the inductance adopted for prediction in the discrete model and the actual inductance. It will intuitively be reflected on the power factors since the reactive power can no longer be controlled to near zero due to the mismatched inductances. The nominal values of grid-side inductor $L_{g,n}$ and PMSG inductor $L_{m,n}$ are set to linearly increase from 50% to 150% of their actual values at the same time inside the controller. The grid-side current THDs are around 3.5% and the PMSM current THDs are around 9.5% if $L_{g,n}$ and $L_{m,n}$ are adopted. When $L_{g,n}$ and $L_{m,n}$ are set to 50% and 150%, grid-side current THDs are around 9.06% and 3.96%, respectively, and the PMSG current THDs are around 15.34% and 11.03%, respectively. As can be seen from Fig. 10, the reactive power, whose 0Var is indicated by the "T" on the left-hand side of it, is always maintained to near 0Var without deviation. The control performance does degrade as the inductances deviate from their actual values, but the system remains stable. Besides, there is no steady-state error in the reactive power even though the mismatched parameters are adopted for prediction.

V. CONCLUSION

In this manuscript, a cascade-free control scheme is proposed for the back-to-back converter-fed PMSM drive system. Instead of using the nested control structure with an outer voltage PI controller, the proposed control scheme regulates the dc-link voltage and power flow directly via one cost function by reconstructing

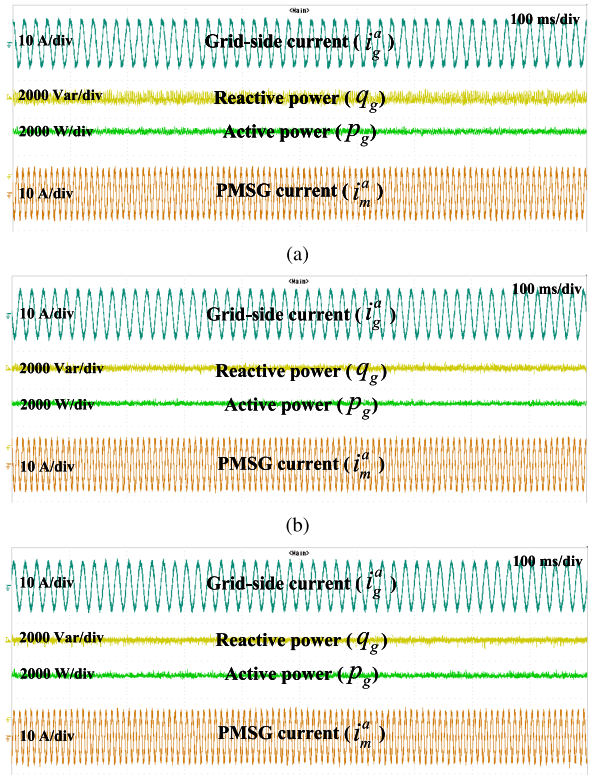

Fig. 10. Experimental results of proposed control scheme with mismatched inductances. (a) $L_{g,n}$ and $L_{m,n}$ is set to 50%($L_{g,n} = 6$ mH and $L_{m,n} = 6$ mH). (b) $L_{g,n}$ and $L_{m,n}$ are adopted ($L_{g,n} = 12$ mH and $L_{m,n} = 12$ mH). (c) $L_{g,n}$ and $L_{m,n}$ are set to 150%($L_{g,n} = 18$ mH and $L_{m,n} = 18$ mH).

its regulation terms. To predict accurately and to improve system robustness under variable parameters, the online corrections for voltage and power expressions are added to remove the steady-state deviation. A series of experimental comparisons against the conventional PI control scheme with modulator, PI-MPC, and modified QC-MPC has confirmed the effectiveness of the proposed control scheme. On the one hand, the proposed control scheme can realize a steady-state performance comparable to that of the PI control scheme with modulator at the same switching frequency. At its rated operating condition, the dc-link voltage ripple is within $\pm$ 3 V and the current THDs are below 3.5 %. On the other hand, the proposed scheme presents a better dynamic response on voltage regulation during the abrupt changes of torque, reactive power, and speed, compared with the other three control schemes. In addition, the proposed control scheme has no steady-state power deviation, which indicates good robustness, even if the mismatched parameters are adopted.

REFERENCES

[1] M. E. Zarei, D. Ramırez, M. Prodanovic, and G. M. Arana, "Model predictive control for PMSG-based wind turbines with overmodulation and adjustable dynamic response time," *IEEE Trans. Ind. Electron.*, vol. 69, no. 2, pp. 1573–1585, Feb. 2022.

[2] A. J. Balbino, B. d. S. Nora, and T. B. Lazzarin, "An improved mechanical sensorless maximum power point tracking method for permanent-magnet synchronous generator-based small wind turbines systems," *IEEE Trans. Ind. Electron.*, vol. 69, no. 5, pp. 4765–4775, May 2022.

[3] S. Ye, D. Zhou, X. Yao, and F. Blaabjerg, "Component-level reliability assessment of a direct-drive PMSG wind power converter considering two terms of thermal cycles and the parameter sensitivity analysis," *IEEE Trans. Power Electron.*, vol. 36, no. 9, pp. 10037–10050, Sep. 2021.

[4] I. Jlassi, J. O. Estima, S. K. El Khil, N. M. Bellaaj, and A. J. M. Cardoso, "Multiple open-circuit faults diagnosis in back-to-back converters of PMSG drives for wind turbine systems," *IEEE Trans. Power Electron.*, vol. 30, no. 5, pp. 2689–2702, May 2015.

[5] S. Xu, S. Tao, W. Zheng, Y. Chai, M. Ma, and L. Ding, "Multiple open-circuit fault diagnosis for back-to-back converter of PMSG wind generation system based on instantaneous amplitude estimation," *IEEE Trans. Instrum. Meas.*, vol. 70, 2021, Art. no. 3512413.

[6] D. Zhou, J. Zhao, and Y. Liu, "Independent control scheme for nonredundant two-leg fault-tolerant back-to-back converter-fed induction motor drives," *IEEE Trans. Ind. Electron.*, vol. 63, no. 11, pp. 6790–6800, Nov. 2016.

[7] M. Shahbazi, P. Poure, S. Saadate, and M. R. Zolghadri, "FPGA-based reconfigurable control for fault-tolerant back-to-back converter without redundancy," *IEEE Trans. Ind. Electron.*, vol. 60, no. 8, pp. 3360–3371, Aug. 2013.

[8] Z. Zhang et al., "Predictive control with novel virtual-flux estimation for back-to-back power converters," *IEEE Trans. Ind. Electron.*, vol. 62, no. 5, pp. 2823–2834, May 2015.

[9] S. Li, T. A. Haskew, R. P. Swatloski, and W. Gathings, "Optimal and direct-current vector control of direct-driven PMSG wind turbines," *IEEE Trans. Power Electron.*, vol. 27, no. 5, pp. 2325–2337, May 2012.

[10] A. Videt, M. Messaoudi, N. Idir, H. Boulharts, and H. Vang, "PWM strategy for the cancellation of common-mode voltage generated by three-phase back-to-back inverters," *IEEE Trans. Power Electron.*, vol. 32, no. 4, pp. 2675–2686, Apr. 2017.

[11] J. Samanes, E. Gubia, X. Juankorena, and C. Girones, "Common-mode and phase-to-ground voltage reduction in back-to-back power converters with discontinuous PWM," *IEEE Trans. Ind. Electron.*, vol. 67, no. 9, pp. 7499–7508, Sep. 2020.

[12] M. Quraan, Q. Farhat, and M. Bornat, "A new control scheme of back-to-back converter for wind energy technology," in *Proc. IEEE 6th Int. Conf. Renewable Energy Res. Appl.*, 2017 pp. 354–358.

[13] A. Yazdani and R. Iravani, "Back-to-Back HVDC conversion system," in *Proc. Voltage-Sourced Converters Power Systems: Model., Control, Appl.*, 2010, pp. 69–107.

[14] I. Jlassi and A. J. M. Cardoso, "Fault-tolerant back-to-back converter for direct-drive PMSG wind turbines using direct torque and power control techniques," *IEEE Trans. Power Electron.*, vol. 34, no. 11, pp. 11215–11227, Nov. 2019.

[15] S. Vazquez, J. A. Sanchez, J. M. Carrasco, J. I. Leon, and E. Galvan, "A model-based direct power control for three-phase power converters," *IEEE Trans. Ind. Electron.*, vol. 55, no. 4, pp. 1647–1657, Apr. 2008.

[16] V. Yaramasu and B. Wu, "Basics of wind energy conversion systems," in *Proc. Model Predictive Control Wind Energy Conver. Syst.*, 2017, pp. 3–58.

[17] F. Grimm, Z. Zhang, and R. Kennel, "Sphere decoding based long-horizon predictive control of three-level NPC back-to-back PMSG wind turbine systems," in *Proc. IEEE Int. Power Electron. Conf.*, 2018, pp. 2895–2900.

[18] T. Geyer, "Predictive control with long horizons," in *Proc. Model Predictive Control High Power Converters Ind. Driv.*, 2016, pp. 195–216.

[19] P. Kou, D. Liang, J. Li, L. Gao, and Q. Ze, "Finite-control-set model predictive control for DFIG wind turbines," *IEEE Trans. Automat. Sci. Eng.*, vol. 15, no. 3, pp. 1004–1013, Jul. 2018.

[20] J. Hu, J. Zhu, and D. G. Dorrell, "Predictive direct power control of doubly fed induction generators under unbalanced grid voltage conditions for power quality improvement," *IEEE Trans. Sustain. Energy*, vol. 6, no. 3, pp. 943–950, Jul. 2015.

[21] Y. Zhang, Z. Li, W. Xu, J. Hu, and J. Zhu, "Grid synchronization of DFIG using model predictive direct power control," in *Proc. IEEE Int. Conf. Elect. Mach. Syst.*, 2011, pp. 1–6.

[22] B. Hu, L. Kang, J. Liu, J. Zeng, S. Wang, and Z. Zhang, "Model predictive direct power control with fixed switching frequency and computational amount reduction," *IEEE Trans. Emerg. Sel. Topics Power Electron.*, vol. 7, no. 2, pp. 956–966, Jun. 2019.

[23] I. Jlassi and A. J. M. Cardoso, "Enhanced and computationally efficient model predictive flux and power control of PMSG drives for wind turbine applications," *IEEE Trans. Ind. Electron.*, vol. 68, no. 8, pp. 6574–6583, Aug. 2021.

[24] J. Rodriguez, J. Pontt, P. Correa, P. Lezana, and P. Cortes, "Predictive power control of an AC/DC/AC converter," in *Proc. IEEE 40th IAS Annu. Meeting. Conf. Rec. 2005 Ind. Appl. Conf.*, 2005, vol. 2, pp. 934–939.

[25] X. Liu, D. Wang, and Z. Peng, "Cascade-free fuzzy finite-control-set model predictive control for nested neutral point-clamped converters with low switching frequency," *IEEE Trans. Control Syst. Technol.*, vol. 27, no. 5, pp. 2237–2244, Sep. 2019.
[26] M. Liu, K. W. Chan, J. Hu, W. Xu, and J. Rodriguez, "Model predictive direct speed control with torque oscillation reduction for PMSM drives," *IEEE Trans. Ind. Inf.*, vol. 15, no. 9, pp. 4944–4956, Sep. 2019.
[27] D. E. Quevedo, R. P. Aguilera, M. A. Perez, P. Cortes, and R. Lizana, "Model predictive control of an AFE rectifier with dynamic references," *IEEE Trans. Power Electron.*, vol. 27, no. 7, pp. 3128–3136, Jul. 2012.
[28] Z. Zhang, F. Wang, T. Sun, J. Rodrıguez, and R. Kennel, "FPGA-based experimental investigation of a quasi-centralized model predictive control for back-to-back converters," *IEEE Trans. Power Electron.*, vol. 31, no. 1, pp. 662–674, Jan. 2016.
[29] J.-Z. Zhang, T. Sun, F. Wang, J. Rodriguez, and R. Kennel, "A computationally efficient quasi-centralized DMPC for back-to-back converter PMSG wind turbine systems without dc-link tracking errors," *IEEE Trans. Ind. Electron.*, vol. 63, no. 10, pp. 6160–6171, Oct. 2016.
[30] J. Rodrıguez, R. M. Kennel, J. R. Espinoza, M. Trincado, C. A. Silva, and C. A. Rojas, "High-performance control strategies for electrical drives: An experimental assessment," *IEEE Trans. Ind. Electron.*, vol. 59, no. 2, pp. 812–820, Feb. 2012.
[31] J. Rodriguez and C. Estay, "Weighting factor design," in *Proc. Predictive Control Power Converters Elect. Drives*, 2012, pp. 3–16.
[32] Z. Zhang, Z. Li, M. P. Kazmierkowski, J. Rodrıguez, and R. Kennel, "Robust predictive control of three-level NPC back-to-back power converter PMSG wind turbine systems with revised predictions," *IEEE Trans. Power Electron.*, vol. 33, no. 11, pp. 9588–9598, Nov. 2018.

Yingjie He (Member, IEEE) received the B.S. degree in electrical engineering from the Shenyang University of Technology, Shenyang, China in 2013, and the M.S. degree in mechatronics engineering from Kyungsung University, Busan, South Korea, in 2016. He is currently working toward the Ph.D. degree with the Institute for Electrical Drive Systems and Power Electronics, Technical University of Munich, Munich, Germany.

His research subject focuses on power electronic converters.

Ying Tang (Member, IEEE) received the B.S. degree in electrical engineering from the Shenyang University of Technology, Shenyang, China in 2013, and the M.S. degree in mechatronics engineering from Kyungsung University, Busan, South Korea, in 2016. She is currently working toward the Ph.D. degree with the Institute for Electrical Drive Systems and Power Electronics, Technical University of Munich, Munich, Germany.

Her research subject focuses on variable-speed motor drives and their control.

Xiaonan Gao (Member, IEEE) received the B.S. and M.S. degrees from the Dalian University of Technology, Dalian, China, in 2013 and 2016, respectively, and the Dr.-Ing. degree from the Technical University of Munich, Munich, Germany, in 2022, all in electrical engineering.

He is currently a Postdoctoral Fellow with the KTH Royal Institute of Technology, Stockholm, Sweden. His research interests include electrical drives, predictive control, multilevel converters, and grid-connected converters.

Haotian Xie (Member, IEEE) was born in Jiangsu Province, China, in 1990. He received the B.S. and M.Sc. degrees in electronic engineering from the Nanjing University of Aeronautics and Astronautics, Nanjing, China, in 2013 and 2017, respectively, and the Ph.D. degree in electrical engineering from the Chair of High-Power Converter Systems, Department of Energy and Process Engineerin, Technical University of Munich, Munich, Germany, in 2023.

He is currently an Associate Professor with the Quanzhou Institute of Equipment Manufacturing, Haixi Institute, Chinese Academy of Sciences, Beijing, China. His research interests include model predictive control, and sensorless control for electrical machine drive system.

Fengxiang Wang (Senior Member, IEEE) was born in Jiujiang, China, in 1982. He received the B.S. degree in electronic engineering and the M.S. degree in automation from Nanchang Hangkong University, Nanchang, China, in 2005 and 2008, respectively, and the Ph.D. degree in electrical engineering from the Institute for Electrical Drive Systems and Power Electronics, Technische Universitaet Muenchen, Munich, Germany, in 2014.

He is currently a Full Professor and the Deputy Director with the Quanzhou Institute of Equipment Manufacturing, Haixi Institute, Chinese Academy of Sciences, Beijing, China. His research interests include predictive control, and sensorless control for electrical drives and power electronics.

Dr. Wang is currently an IET Fellow and an Associate Editor for IEEE TRANSACTIONS ON INDUSTRIAL ELECTRONICS and IEEE TRANSACTIONS ON ENERGY CONVERSION. As the General Chair, he organized IEEE 5th International Symposium on Predictive Control of Electrical Drives and Power Electronics.

Ralph Kennel (Senior Member, IEEE) was born in Kaiserslautern, Germany, in 1955. He received the Diploma and Dr.-Ing. (Ph.D.) degrees in electrical engineering from the Technical University of Kaiserslautern, Kaiserslautern, in 1979 and 1984, respectively.

From 1983 to 1999, he was on several positions with Robert BOSCH GmbH, Gerlingen, Germany. Until 1997, he was responsible for the development of servo drives. From 1994 to 1999, he was a Visiting Professor with the University of Newcastleupon-Tyne, Tyne, U.K. From 1999 to 2008, he was a Professor of electrical machines and drives with Wuppertal University, Wuppertal, Germany. Since 2008, he has been a Professor of electrical drive systems and power electronics with Technische Universtaet Muenchen, Munich, Germany. His research interests include sensorless control of ac drives, predictive control of power electronics, and hardware-in-the-loop systems.

Dr. Kennel is a Fellow of IEE and a Chartered Engineer in the U.K. Within IEEE, he is a Treasurer of the Germany Section as well as ECCE Global Partnership Chair of the Power Electronics Society.